Chemical Geology 411 (2015) 260–273

Contents lists available at ScienceDirect

Chemical Geology

journal homepage: www.elsevier.com/locate/chemgeo

# Pore-scale heterogeneity in the mineral distribution and reactive surface area of porous rocks

Peter Lai *, Kevin Moulton, Samuel Krevor

*Department of Earth Science & Engineering, Imperial College, London SW7 2BP, UK*

ARTICLE INFO

*Article history:*
Received 12 November 2014
Received in revised form 4 July 2015
Accepted 6 July 2015
Available online 10 July 2015

*Keywords:*
Reactive transport
Heterogeneity
Surface area
Micro-tomography

ABSTRACT

The reactive surface area is an important control on interfacial processes between minerals and aqueous fluids in porous rocks. Spatial heterogeneity in the surface area can lead to complications in modelling reactive transport processes, but quantitative characterisation of this property has been limited. In this paper 3D images obtained using X-ray micro-tomography were used to characterise heterogeneity in surface area in one sandstone and five carbonate rocks. Measurements of average surface area from X-ray imagery were 1–2 orders of magnitude lower than measurements from nitrogen BET. A roughness factor, defined as the ratio of BET surface area to X-ray based surface area, was correlated to the presence of clay or microporosity. Co-registered images of Berea sandstone from X-ray and energy dispersive spectroscopy imagery were used to guide the identification of quartz, K-feldspar, dolomite, calcite and clays in X-ray images. In Berea sandstone, clay and K-feldspar had higher average surface area fractions than their volumetric fractions in the rock. In the Edwards carbonate, however, modal mineral composition correlated with surface area. By sub-sampling digital images, statistical distributions of the surface area were generated at various length scales of subsampling. Comparing these to distributions used in published modelling studies showed that the common practice of leaving surface area and pore volume uncorrelated in a pore has lead to unrealistic combinations of surface area and pore volume in the models. We suggest these models adopt a moderate correlation based on observations. In Berea sandstone, constraining ratios of surface area to pore volume to a range of values between that of quartz-lined and five times that of clay-lined spheres appeared sufficient.



## 1. Introduction

The flow of aqueous fluids through porous rocks concurrent with chemical reactions is a dominant feature of many natural and engineered processes. These include the formation of karst zones, the evolution of snow packs during melting, $CO_2$ subsurface injection, nuclear waste remediation, near-surface contaminant transport and remediation and the transport of magma through the mantle. Reviews of reactive transport processes can be found in Steefel et al. (2005) and Steefel and Maher (2009). Such processes are particularly difficult to model due to the coupling of chemical reactions, reactant transport through the pore space, and at times, the evolution of the pore space itself through rock dissolution and mineral precipitation (Haggerty and Gorelick, 1995; Lichtner and Kang, 2007; Dentz et al., 2011; Boso and Battiato, 2013). As a result, there are longstanding difficulties with the use of laboratory scale characterisation of rock samples for modelling of transport and reaction at the field scale (Velbel, 1985; Malmström et al., 2000; White and Brantley, 2003; Zhu, 2005; Maher et al., 2006; Navarre-Sitchler and Brantley, 2007).

Recent investigation at pore and pore-network scales has begun to reveal the dominant underlying physical processes giving rise to the macroscopic manifestation of reaction at the pore scale. Laboratory scale observations of dissolution and precipitation reactions at mineral surfaces are precise and rate laws that include correlations with fluid chemistry and temperature are repeatable. Thus, Flukiger and Bernard (2009) and Molins et al. (2012) have accurately modelled upscaled reactive transport processes, fully resolving processes of flow, chemical component transport and reaction throughout a three-dimensional pore space. Computational power, however, limits direct modelling combining flow with heterogeneous chemical reaction to spatial domains of a few millimetres.

Statistical descriptions of rock properties – porosity, mineral composition, reactive surface area – that are heterogeneous at the pore scale provide a link between those processes at the pore scale that can be directly modelled and the larger scale characterisation of reactive

* Corresponding author.
*E-mail address:* p.lai12@imperial.ac.uk (P. Lai).

http://dx.doi.org/10.1016/j.chemgeo.2015.07.010

transport relevant to the field. They provide a description of the heterogeneity that gives rise to the complex reaction dynamics and deviations from continuum scale descriptions. Several groups have made use of such statistical descriptions of a porous medium for pore-network models of reactive transport processes (Li et al., 2007; Peters, 2009; Nogues et al., 2013; Raoof et al., 2013). It is possible that such descriptions could also be used to parameterise multi-continuum models or single continuum models with more appropriate effective parameters (Lichtner and Kang, 2007). In general these approaches have been limited, however, in their ability to base the statistical properties on direct observations of the properties in the rock material themselves.

In this work, we have focused on creating statistical descriptions of reactive surface area heterogeneity from X-ray microtomography observations of one sandstone and five carbonate rocks. Many studies have shown the important role of the surface area of reacting minerals – the fluid–solid interface – in determining rates and extents of reaction in porous rocks (Helgeson et al., 1984; Velbel, 1985; Haggerty and Gorelick, 1995; Kieffer et al., 1999; Colon et al., 2004; Luquot and Gouze, 2009; Noiriel et al., 2009; Gouze and Luquot, 2011; Navarre-Sitchler et al., 2013).

The observation of surface area, and its distribution among specific mineral phases in a porous medium, however, has been complicated by the difficulty in interrogating the interior properties of a rock. Conventionally, the approach for characterising surface area in field settings has been to measure overall surface area using, e.g., $N_2$-BET, and correlate mineral specific surface area to modal composition (Helgeson et al., 1984; Velbel, 1985; Zhu, 2005; Kampman et al., 2009). Observations of the rates of reactions in rock cores with simple mineralogy – pure quartz, calcite – and well established rate laws have also been used in Kieffer et al. (1999), Colon et al. (2004), Noiriel et al. (2009), and Luquot and Gouze (2009) to infer the evolution of surface area in sandstone and carbonate rocks. Neutron scattering has been used by Navarre-Sitchler et al. (2013) to characterise surface area heterogeneity and its evolution with reaction in low-porosity igneous rocks. That technique had the advantage that features with length scales from microns to nanometers are simultaneously characterised across a sample domain with a length scale of order 1 cm.

Recent work by Peters (2009), Landrot et al. (2012), Golab et al. (2013) and Hezel et al. (2013) have described the distribution of surface area from observations of rocks using X-ray and electron imaging. In those works they pioneered the combined use of these observations, registering 3D X-ray imagery of rocks at the microscopic scale with 2D electron image mapping of minerals to produce 3D maps of the mineral distribution within a rock. The success of these techniques suggested that there was an opportunity to derive these statistical descriptions of the pore space from direct imagery of the mineral phases in situ of the rocks themselves. In this work we endeavoured to apply those techniques to develop a statistical description of the heterogeneity in the mineral surface area available for reaction from direct observations of a Berea sandstone and five carbonate rocks. The rock samples were dominated by pore-network structures, absent fractures, dissolution features, and vuggy conduits for flow. The description of these structures will be key to a full description of reactive processes in porous media, but is outside the scope of this work.

In this paper the materials and methods employed for the research are reviewed in Section 2. This includes brief summaries of the use of conventional petrological characterisation tools and more detail about the techniques used for processing X-ray images. The results are presented in Section 3. This includes detailed comparison between rock properties observed from conventional techniques to the same properties calculated from the X-ray imagery. Statistical descriptions of the mineral surface area are presented and compared to properties assumed in the network modelling study of Li et al. (2007). A significant utility of this work is the data itself and extensive supplemental information has been included with this paper.

## 2. Materials and methods

### 2.1. Rock samples

The rocks studied are shown in scanning electron microscope images in Fig. 1. The samples included two types that have been used extensively in petrophysical research applications, Berea sandstone (Khilar and Fogler, 1983; Churcher et al., 1991; Shaw et al., 1991) and Estaillades limestone (Cadoret et al., 1995; Bijeljic et al., 2013). In addition, four quarry limestones, Ketton, Indiana, Guelph and Edwards, were chosen to explore the impact of pore structure on heterogeneity in the surface area.

The Berea sandstone and the Edwards and Guelph carbonates had significant fractions of at least two mineral types. For this reason mineral-specific characterisation was performed for the Berea and Edwards and not on the Estaillades, Ketton and Indiana carbonates. These were nearly entirely calcite and they were treated as monomineralogical systems in the analysis of surface area.

### 2.2. Average chemical and mineral composition

Observations made with X-ray diffraction (XRD) were used to identify the major minerals present in the samples and X-ray fluorescence spectrometry (XRF) was used to deduce approximate mineral fractions from the bulk chemical composition. The specimens for XRD and XRF were taken separately from the same sample blocks. The instrument used for XRD analysis was a PANalytical X'Pert Pro MPD. Quantitative XRF was performed on 38 mm diameter, 10 mm thick, solid disc specimens using a wavelength dispersive XRF spectrometer, Bruker AXS S4 Explorer. The elemental compositions from the XRF measurements were used to produce an estimate of mineral mass fractions based on the minerals identified by XRD in a procedure detailed in Appendix A of the Supplemental Information.

### 2.3. Specific surface area and porosity

Surface area quantification from micro CT imagery was compared with parallel observations on the same samples using nitrogen adsorption and the Brunauer–Emmett–Teller (BET) method. Since the introduction of the concept of reactive surface area by Helgeson et al. (1984), a more nuanced understanding of the reactive surface area has developed. The use of BET surface areas, however, is still the observation of choice for calculating and modelling field scale water–rock interactions (Zhu, 2005; Kampman et al., 2009). It has also been shown to be a useful proxy for effective surface area in far from equilibrium reaction processes (Hanchen et al., 2007). Normalisation of surface areas calculated from X-ray images in this work by those observed using $N_2$ BET also allows for comparison with past studies and wider application in the use of the observations in modelling.

The specific surface area of cylindrical pieces of each rock was measured, with samples sized so that they could also be imaged in the micro X-ray CT. The dimensions of the samples were approximately 5 mm diameter and 20 mm length. The analysis was performed with a Micromeritics Tristar 3000 using nitrogen as the working gas.

A nitrogen porosimeter was used to measure the average porosity of samples. The instrument was a Vinci Technologies PoroPerm Production 2. The samples were right cylinders, 1 in. (2.54 cm) each in diameter and length.

Mercury intrusion porosimetry (MIP) was used to characterise the pore throat and size distribution of the rock samples. The pore throat distribution was used to estimate the fraction of the total pore space below the resolution of the X-ray CT images (Knackstedt et al., 2008). This resolvable porosity was then used to back calculate the expected resolvable

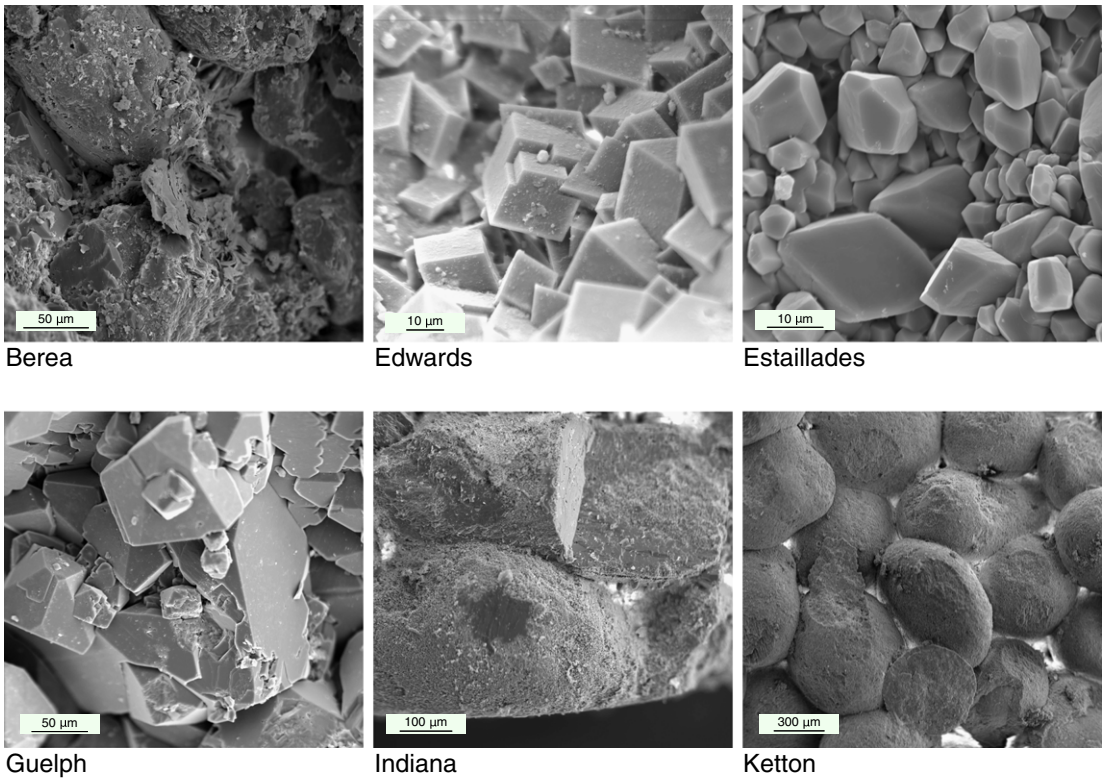


**Fig. 1.** Secondary electron photomicrographs of the rocks used in this study. There was no obvious difference between the imagery of the various Berea samples used in this work.

porosity from CT imagery at 1 μm resolution for evaluation of the segmentation process. The measurements were made on an AutoPore IV 9500 (Micromeritics Instrument Corp., Norcross, GA, USA) using 1–2 g of rock fragments. The pressure ranged from 0.5 psi to 33,000 psi. The intrusion volume was normalised to the maximum intrusion volume at 33,000 psi to obtain saturation. Pore radius, titr was calculated as a function of capillary pressure, $P_c$ according to Eq. (1), where the interfacial tension, $\sigma_{hg\ -\ air}$ is 485 dyn/cm, and the contact angle, $\theta_{hg\ -\ air}$ is 140° for sandstone and 130° for carbonate (Ethington, 1990).

$$P_c = \frac{2\sigma_{hg-air}\cos\theta_{hg-air}}{r} \quad (1)$$

The radius in Eq. (1) does not refer to a pore body radius, but rather a limiting radius for mercury intrusion — a pore throat. Thus to approximate 1 μm pore bodies we use a value of $r = 0.1$ μm from the mercury intrusion data, assuming that pore bodies are approximately an order of magnitude larger than pore throats.

### 2.4. Electron imaging and spectroscopy

Electron microscopy and spectroscopy were used to provide two-dimensional chemical and mineral phase maps of the Berea sandstone and Edwards carbonate. This provided a guide for segmenting mineral groups in X-ray images in these rocks. Images were taken on a JEOL JSM-6400 SEM. The mineral composition of Berea sandstone, and Edwards and Guelph carbonates were investigated using the backscattered electron (BSE) imaging mode. Energy dispersive spectroscopy (EDS) was used to generate elemental maps for the identification of mineral groups, chlorite, clay, and feldspar. Previous efforts (Peters, 2009; Landrot et al., 2012) have used thresholded BSE and EDS maps successfully to generate maps of the mineral distribution and a similar approach was used here. The mineral-volume and surface area fractions were estimated from the elemental maps. The phases present in the Berea sandstone were divided into five broad groups: *pore*, *clay minerals*, *quartz*, *feldspars*, and *others* to correspond with groups that could be identified in the X-ray images, discussed in the following Section 2.5. Specific parameters used for segmenting the electron images are provided in Appendix B of the Supplemental Information.

### 2.5. X-ray imaging and image processing

In an image reconstructed from X-ray tomography, the value assigned to each volume pixel, or voxel, represents the average X-ray attenuation property of the material in that volume. The degree of attenuation is determined by the elemental composition and bulk density of the material and this gives the potential for limited mineral phase identification in X-ray images. Work in Uesugi et al. (1999) and Tsuchiyama et al. (2000, 2005, 2013) showed that quantitative measurements of X-ray linear attenuation coefficients (LAC) were possible with both mono- and poly-chromatic X-ray beams. Based partly on these principles, several groups have recently made use of laboratory micro CT devices in application to mineral identification in rocks, including Peters (2009), Landrot et al. (2012), Golab et al. (2013) and Hezel et al. (2013).

The general procedure for segmentation – both between pore and solid, and of the mineral groups in the case of the Berea sandstone and Edwards carbonate – is described here and detailed information is provided in Appendix C of the Supplemental Information. For all rocks, the X-ray image was denoised using the "non-local means neighbourhood" filter in Avizo Fire 8.0. The watershed segmentation module in Avizo Fire 8.0 was used for both binary and multiphase segmentation. Grey scale thresholds for the seeds were selected by eye and the specific parameters for each rock are provided in Appendix C of the Supplemental Information. Additionally, the digital image after denoising is provided in the Supplemental Information so

that others may repeat the segmentation or implement their own procedures.

With the Berea sandstone and Edwards carbonate, the solid phase was further segmented into mineral groups. The work reported in Latham et al. (2008), Sok et al. (2010), and Golab et al. (2013) demonstrated the value of simultaneous analysis by backscattered electron imaging (BSE), energy dispersive spectroscopy (EDS), and micro-computed X-ray tomography for the use of X-ray CT for mineral phase and rock structure characterisation. We employed a similar approach, comparing data from X-ray imagery, BSE imaging, and 2D elemental composition maps to guide and evaluate the effectiveness of mineral identification using X-ray imagery. To create co-registered images, a Berea sandstone specimen was imaged in the X-ray microscope using the parameters described in Appendix C of the Supplemental Information. Then, the sample was cut to expose a section of the rock that was imaged, and the remaining sample impregnated with epoxy and polished for BSE and EDS analysis as described in Section 4. The cut sample was imaged again to establish the location of the exposed surface. The alignment and registration of both X-ray images was performed in Avizo Fire 8.0. A range of grey scale values were associated with each mineral grouping based on an identification of those minerals in a particular slice of the image. These were used to identify the seeds for the watershed segmentation process.

Tables 1 and 2 summarise the definition of the segmentation groups for the Berea sandstone and Edwards dolomite, respectively. The *feldspar* group mostly consists of alkali feldspars but plagioclase, illite, and muscovite were also included in this group. Kaolinite and smectite comprised the bulk of the *clay* mineral group. The *quartz* group consisted of quartz and albite which has similar attenuation properties to quartz. Calcite, oxides and sulphides such as hematite and pyrite, and remaining micas, including biotite, formed the *others* group. Phase contrast effects at the grain boundaries in the Berea sandstone often resulted in misidentification of quartz as small pieces of feldspar. The *feldspar* volumes were sorted by size and feldspar labels below a size threshold were relabelled as quartz. The central $600^3$ voxels were extracted from the centre of the image for further analysis. The mineral groups identified in the Edwards rock were *quartz*, *dolomite*, and *others*.

### 2.6. Quantifying surface area heterogeneity

In this work we have focused on describing spatial heterogeneity in the surface area of a rock through the construction of distributions in the local surface area to pore volume ratio. There are a number of ways in which surface area heterogeneity could be quantified (we note that the data, available as supporting material, can be used to generate these). This metric reflects a contribution to the local reactivity of the solid in this system *per unit volume of fluid*.

We have used this metric for a number of reasons. The amount of surface area available in a sub-region of a rock is influenced both by the presence of porosity and the shape of the pore-solid boundary. In other words, a given cubic millimetre of rock may have more surface area than a comparative sub-volume in a separate location because it has more pore volume, or it may have more surface area because the geometry of the pore itself is more tortuous. The comparison of the surface area to pore-volume ratio disentangles these and provides a measure of solid reactivity due to surface area morphology alone.

It is also evident that reactive transport processes are strongly effected by feedbacks between the changing composition of the fluid and reaction rates at the fluid–solid boundary (Colon et al., 2004; Noiriel et al., 2009; Dentz et al., 2011; Gouze and Luquot, 2011; Menke, 2015). The surface area to pore (fluid) volume ratio provides some measure of the extent to which local reactive processes will influence the local chemical composition of the fluid — there is less fluid chemistry change in a large body of fluid compared with a smaller body for a given reaction rate (Lichtner and Kang, 2007).

To build the distribution from an X-ray image, first an image was sub-sampled at a chosen length scale. From this subsample the surface area to pore volume ratio was calculated following a procedure detailed in Appendix D of the Supplemental Information. Then the process was repeated for every unique location throughout the X-ray image and a frequency histogram was constructed from the values. For example, an X-ray image cube with dimension 600 μm on each side contained 216 unique sub-cubes with dimension 100 μm on each side. Frequency histograms were generated for each rock type using sub-sample sizes ranging from 50 μm to 300 μm. For all of the rocks, initially this process was performed using a binary segmentation of the images into pore space and rock. Subsequently, the distributions for the Berea sandstone and Edwards carbonate were separated into their individual mineral constituents.

**Table 1**
Description of the X-ray segmentation groups for the Berea sandstone. Minor minerals constituted less than 10% of a given segmentation group.

| Group name | Major mineral | Minor minerals |
|---|---|---|
| Feldspar | Alkali feldspar | Plagioclase, illite, muscovite |
| Quartz | Quartz | Albite |
| Clay | Kaolinite | Smectite |
| Other | Calcite | Hematite, pyrite, mica |

**Table 2**
Description of the X-ray segmentation groups for the Edwards dolomite. Minor minerals constituted less than 10% of a given segmentation group.

| Group name | Major mineral | Minor minerals |
|---|---|---|
| Quartz | Quartz | Clay |
| Dolomite | Dolomite, calcite | Ankerite |
| Other | Hematite, pyrite | |

## 3. Results

### 3.1. Porosity and surface area

Fig. 2 shows the pore throat size distribution estimated from mercury intrusion porosimetry. The corresponding estimate of the fraction of the total pore space below the resolution of the X-ray CT images is shown in Fig. 3. Recall from Section 3 that the cutoff for the unresolvable pore volume corresponded to a radius of 0.1 μm on the MIP plot, assuming that pore bodies were approximately ten times larger than pore throats. It was estimated that the X-ray imagery could capture 90–95% of the porosity for the Berea sandstone and Estaillades and Guelph carbonates whereas significant amounts of unresolvable "microporosity" was present in the Edwards, Ketton, and Indiana carbonates. In the case of the Ketton carbonate, Fig. 2 shows a clear bimodal distribution of the pore throats with approximately 40% of the porosity accessed through pore throats greater than 10 μm and another 40% below $10^{-1}$ μm. The Guelph and Indiana carbonates have multiple modes with porosity more evenly distributed across the length scales.

Fig. 4 shows the porosity estimate from the steady-state nitrogen gas porosimetry data compared with micro CT imagery, before and after correcting the micro CT based calculation for the sub-resolution porosity. The corrected values are simply the uncorrected values divided by the fraction of resolvable porosity shown in Fig. 3. In all cases the porosity calculation based on CT imagery alone underestimated the porosity relative to porosimetry, as expected. Only in the case of the Edwards and Ketton carbonates does the correction significantly reduce the difference.

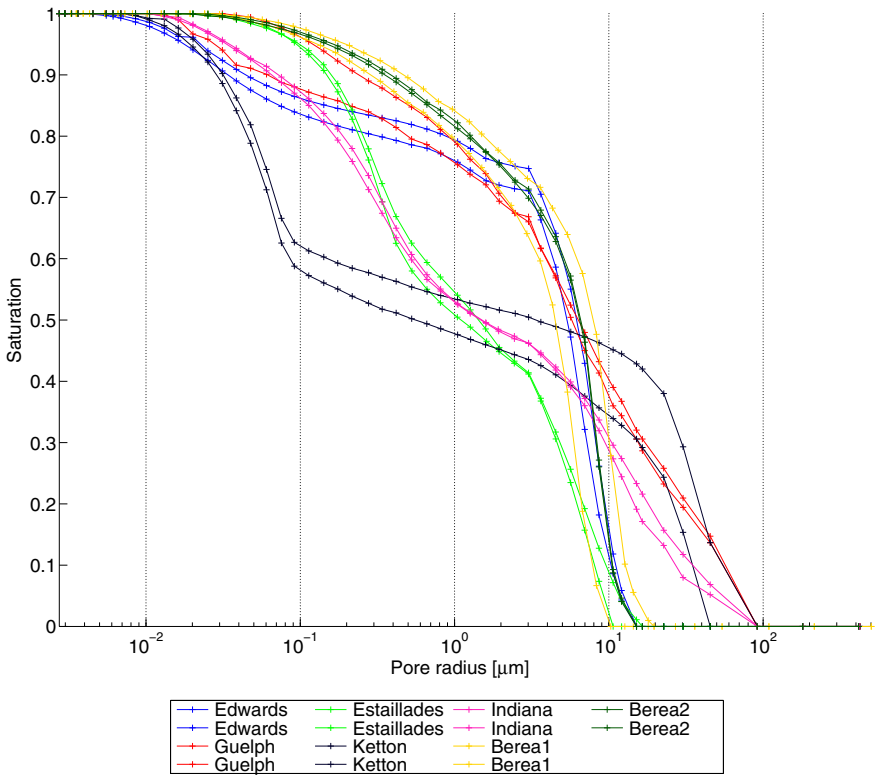


**Fig. 2.** Mercury saturation as a function of pore radius for sandstone and carbonate samples used in this study. Each measurement was repeated on two separate specimens.

The vast difference in size scale between samples used in each measurement (0.2 $mm^3$ in the X-ray imagery as compared with about 100 $cm^3$ for the porosimetry observation) means that discrepancies were to be expected. An indication of the variability in the porosity measurement for the Berea sandstone is shown for the Berea 2 sample. For this sample 20 X-ray images were generated and the corresponding porosity variation is shown as whiskers from the mean value in Fig. 4. A range of porosity values varying over 0.10 porosity units was observed due to natural heterogeneity in the rock at the size scale of the X-ray images, apparently below the representative elementary volume for porosity. Porosity from nitrogen gas porosimetry and the pore throat size distributions measured from mercury intrusion porosimetry, on the other hand, showed little variation due to the larger volume of the samples.

Fig. 5 shows that the BET surface area of the rocks ranged nearly two orders of magnitude, from .08 $m^2\ g^{-1}$ for the Guelph carbonate up to 4.3 [$m^2\ g^{-1}$] for the Edwards carbonate. The surface area of Berea sandstone samples varies within the range of 0.7–1.4 $m^2\ g^{-1}$, similar to values that can be found in the literature, e.g., (Sen et al., 1990).

In the work of (Kerbrat et al., 2008) it was shown that the calculation of specific surface area from X-ray CT images converges to adsorption based measurements when the roughness of the surfaces is above the resolution of the X-ray imagery. For the minerals studied in this work it was expected that a significant fraction of surface area would be below the resolvable threshold of the 1 μm resolution micro CT imagery. Fig. 6a shows pairs of BET and micro CT based surface area measurements obtained from a single sample. The values are provided in tabular form in Appendix E of the Supplemental Information. The BET surface areas were 1–2 orders of magnitude higher than the values calculated from the X-ray imagery. There was a weak correlation among the entire dataset. This is primarily due to the varying degrees that specific mineral groups and microporous regions contribute to the discrepancy between the two observations for a given rock.

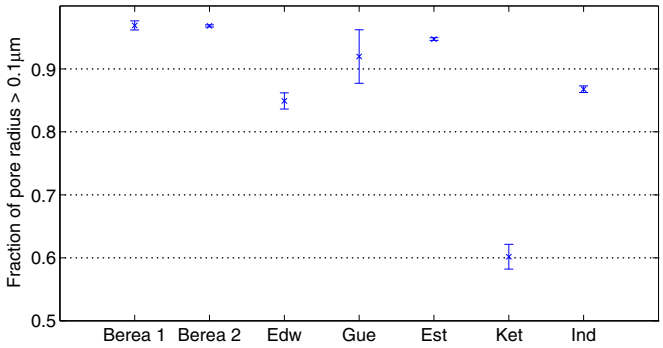


**Fig. 3.** Resolvable porosity in CT images for the sandstone and carbonate samples used in this study estimated from mercury intrusion porosimetry.

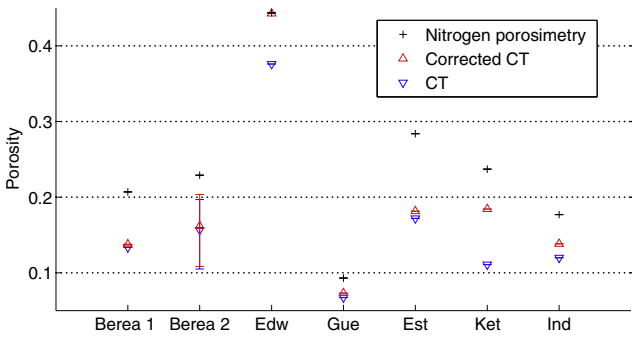


**Fig. 4.** Comparison of porosity measured from nitrogen gas porosimetry and micro CT imagery at 1 μm resolution, before and after correction.

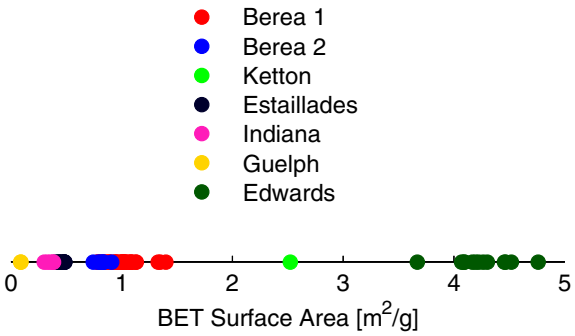


**Fig. 5.** The BET specific surface areas of the rocks used in this study.

The comparison of X-ray imagery to surface adsorption measurements leads to a variation of the concept of the roughness parameter. The roughness parameter is an empirical factor conventionally used to reconcile the difference between surface areas measured with adsorption and those calculated based on the assumption of a simplified mineral grain geometry, e.g., a sphere (Helgeson et al., 1984; White and Peterson, 1990). In the case of this work, the X-ray image provides the geometrical simplification. On the one hand X-ray imagery can provide more morphological information than, e.g., the assumption of spheroid grains, because more complex shapes are resolved in the imagery. On the other hand, there is no limit to the grain or pore size considered in the purely geometrical framework (one can assume spheres as small as is known to be appropriate) whereas with the X-ray imagery micro porous regions can only be accounted for with the roughness parameter.

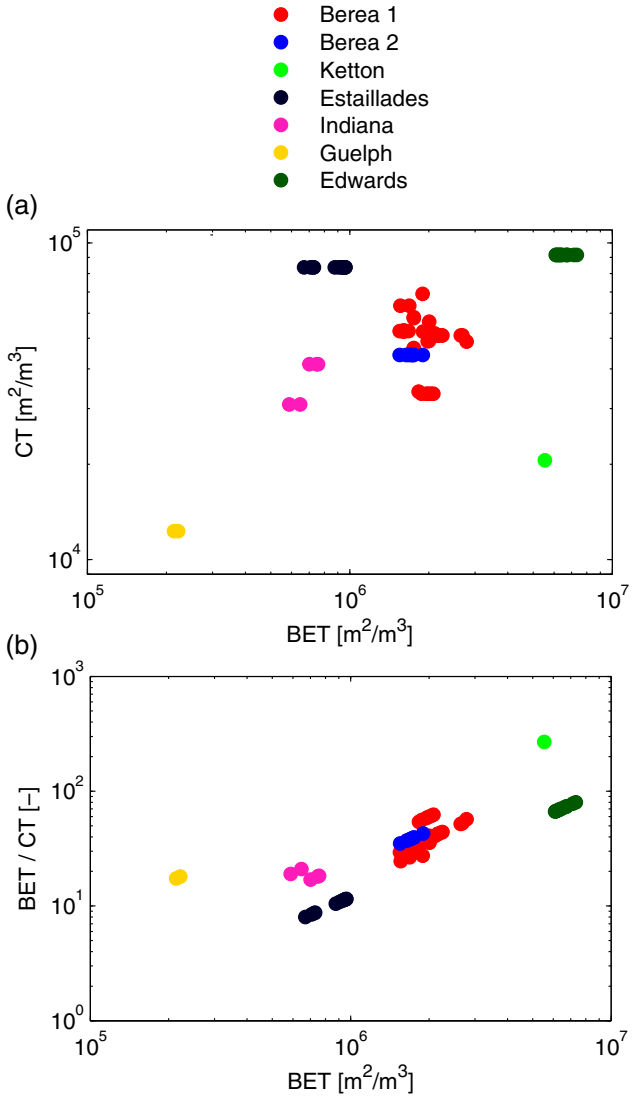


**Fig. 6.** (a) Surface area inferred from CT observations is plotted against the measurement using $N_2$ BET. (b) The roughness ratio (BET surface area: CT calculated surface area) plotted against BET surface area. This shows that roughness increases as expected with total BET surface area. Variation among sample types at a constant BET surface area reflects differences in microporosity between e.g., the Edwards and Ketton or the Indiana and Estaillades.

**Table 3**
Minerals identified from X-ray diffraction in the rock samples used in this work.

| Sandstone | Quartz | Kaolinite | Dolomite | Orthoclase | Microcline |
|---|---|---|---|---|---|
| Berea | ✓ | ✓ | ✓ | ✓ | ✓ |
| Carbonates | Calcite | Dolomite | Ankerite | Quartz | |
| Edwards | ✓ | ✓ | ✓ | ✓ | |
| Estaillades | ✓ | | | | |
| Guelph | | ✓ | ✓ | | |
| Indiana | ✓ | ✓ | | | |
| Ketton | ✓ | ✓ | | | |

In Fig. 6b the ratio of the two surfaces areas, the roughness parameter, is plotted as a function of the BET surface area. As expected, the roughness of the samples generally increases with increasing total surface area. Roughness factors based on geometrical shapes alone have been observed to range from 5–200 for unpolished mineral grains in rocks (White and Peterson, 1990) similar to the range obtained in this work. The coincidence may reflect the competing effects of increased geometrical complexity balanced by the lack of the resolved microporosity.

A comparison of the roughness parameter plot (Fig. 6b) with the MIP based analysis of resolvable porosity (Fig. 3) provides insight into the nature of the roughness for the various rocks. The Ketton carbonate has the highest roughness factor and also the most sub-resolution pore space: nearly 40% of the pore volume was expected to be below the resolution of the X-ray imagery. This is followed by the Edwards carbonate in both roughness and microporosity. In these cases, microporosity is thus likely to be a major contributor to the roughness ratio. Following this, the Berea sandstone has the next highest roughness factor but among the most resolvable porosity. Over 90% of the pore space was estimated to be above the X-ray image resolution. In this case the roughness must be primarily attributed to the high clay content of the rock. The Guelph and Indiana carbonates have minor amounts of microporosity, no clay and correspondingly low roughness factors. The Estaillades has the least amount of microporosity of the carbonates and has the lowest roughness ratio of the group, despite having an equal or higher BET surface area compared with the Guelph and Indiana carbonates. This further underscores the role that microporosity plays in the discrepancy between the X-ray images and the BET measurements for the carbonate minerals. In

**Table 4**
The major elemental composition by mass fraction of sandstone and carbonate rocks measured using X-ray fluorescence spectroscopy. The units are weight percent.

| Sandstone | Si | Al | K | Fe | Ca | Ti | Mg | Na |
|---|---|---|---|---|---|---|---|---|
| Berea 1 | 84.88 | 5.33 | 3.49 | 2.49 | 2.11 | 1.11 | 0.36 | 0.23 |
| Berea 2 | 81.48 | 5.04 | 3.57 | 3.88 | 4.16 | 1.03 | 0.61 | 0.22 |

| Carbonates | Ca | Mg | Fe | Si | K | Na | Al |
|---|---|---|---|---|---|---|---|
| Edwards | 72.99 | 14.83 | 2.01 | 5.31 | 2.75 | 0.00 | 2.11 |
| Estaillades | 99.30 | 0.37 | 0.14 | 0.15 | 0.00 | 0.00 | 0.05 |
| Guelph | 75.13 | 24.03 | 0.20 | 0.24 | 0.10 | 0.16 | 0.14 |
| Indiana | 98.74 | 0.55 | 0.32 | 0.25 | 0.14 | 0.00 | 0.00 |
| Ketton | 97.01 | 0.82 | 1.52 | 0.36 | 0.04 | 0.00 | 0.24 |

**Table 5**
Mineral composition by mass fraction of Berea sandstone and carbonate samples inferred from the XRF data. The units are weight percent.

| | Sandstone | | Carbonate | | | | |
|---|---|---|---|---|---|---|---|
| | Berea 1 | Berea 2 | Edwards | Estaillades | Guelph | Indiana | Ketton |
| Dol | 0.2 | 0.4 | 45.4 | 0 | 64.8 | 0 | 0 |
| Ank | 0.7 | 1.3 | 0 | 0 | 0 | 0 | 0 |
| Cal | 1.3 | 2.9 | 47.0 | 99.6 | 35.2 | 99.2 | 98.3 |
| Qtz | 73.1 | 70.3 | 7.6 | 0.4 | 0 | 0.8 | 1.7 |
| Or | 13.1 | 12.6 | 0 | 0 | 0 | 0 | 0 |
| Ab | 1.0 | 1.0 | 0 | 0 | 0 | 0 | 0 |
| An | 1.7 | 1.5 | 0 | 0 | 0 | 0 | 0 |
| Kln | 2.1 | 1.6 | 0 | 0 | 0 | 0 | 0 |
| Ill | 1.7 | 2.4 | 0 | 0 | 0 | 0 | 0 |
| Sme | 2.3 | 1.9 | 0 | 0 | 0 | 0 | 0 |
| Chm | 0.7 | 1.0 | 0 | 0 | 0 | 0 | 0 |
| Clc | 0.3 | 0.5 | 0 | 0 | 0 | 0 | 0 |
| Py | 1.7 | 2.6 | 0 | 0 | 0 | 0 | 0 |

other words, with the carbonate rocks, high specific surface areas in the absence of microporous regions were well captured by the X-ray imagery.

### 3.2. Chemical and mineral composition

The minerals identified by XRD in the rocks are shown in Table 3, the bulk chemical compositions are shown in Table 4 and the inferred mineral compositions are shown in Table 5.

**Table 6**
Mineral volume and area fraction from co-registered CT and SEM slice of Berea sandstone (see Fig. 7).

| | Volume fraction | | Area fraction | |
|---|---|---|---|---|
| | CT | SEM | CT | SEM |
| Clay | 0.07 | 0.12 | 0.82 | 0.29 |
| Quartz | 0.85 | 0.77 | 0.17 | 0.49 |
| Feldspar | 0.08 | 0.10 | 0.01 | 0.21 |
| Others | 0.01 | 0.01 | 0 | 0.02 |

Results showing details of the image processing of the BSE and X-ray imagery are reported in Appendix B and C of the Supplemental Information. To guide the X-ray image processing for the Berea sandstone, segmentation was performed on locations in the rock that had been imaged using BSE. The comparative segmentation is shown in Fig. 7.

The volume and area fractions of minerals in the images derived from BSE and X-ray observations for the same location in the rock are summarised in Table 6. The porosity and specific surface area inferred from the co-registered images are recorded in Table 7.

The segmentation of the X-ray image identified quartz, K-feldspar and most clays well. In this particular location there was significant albite (cyan in the BSE image in Fig. 7) which was included in the quartz segmentation group because it could not be distinguished in the X-ray images from grey-scale segmentation. At the bottom centre of the slice, there is a large orthoclase grain that has been partially weathered to illite and was identified as feldspar and quartz in the X-ray image. In this rock, the illite and albite minerals constitute less than 10% of the

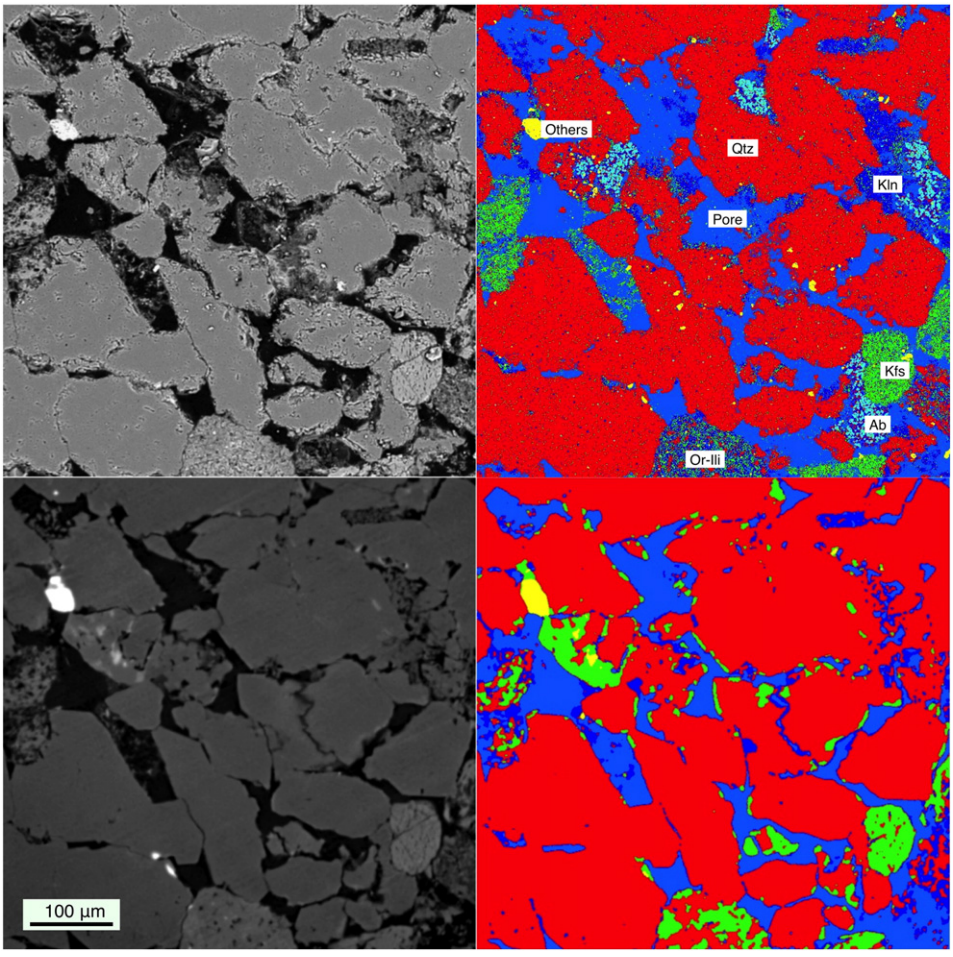


**Fig. 7.** On the left is the BSE image (top), and micro CT (bottom) of a Berea sandstone. On the right is the segmented BSE (top), and segmented micro CT image (bottom). In the segmented BSE image, sodium feldspar is in cyan, distinct from the potassium feldspars in green.

**Table 7**
Porosity and surface area per pore volume from co-registered CT and SEM slice of Berea sandstone (see Fig. 7).

| | CT | SEM |
|---|---|---|
| Porosity | 0.148 | 0.151 |
| Total surface area / pore volume [$\mu m^2/\mu m^3$] | 0.234 | 0.349 |

total segmentation grouping (see Table 5) implying that this location saw a larger impact than would be typical for the image as a whole.

Whilst the volume estimates are largely consistent, the surface area estimates are not. In particular, the estimates from the X-ray image show a far higher clay surface area fraction, and lower quartz and feldspar fraction compared with the SEM. The discrepancy appears to arise predominantly from a combination of the higher resolution of the SEM image with the significant fraction of surface area apparent in the interior of grains that is not visible in the X-ray imagery.

The volumetric composition of the entire Berea sandstone and Edwards carbonate X-ray images in terms of the segmentation mineral groups are provided in Table 8 alongside the surface area fraction calculated from the images. This can be compared with the volumetric fraction of the mineral groups measured by XRF in Table 5. For the sandstone, the inferences from X-ray imagery appear to underestimate the feldspar group minerals and overestimate the quartz group minerals whilst the clay group is consistent. For the Edwards carbonate, the X-ray imagery appears to overestimate the amount of quartz at the expense of the carbonate minerals.

Comparing the volumetric fraction and surface area fraction of the minerals from the X-ray imagery of the Berea sandstone shows that there was little correlation between the two. In all of the samples, the clay and feldspar group demonstrated far higher surface area fractions compared with the bulk mineralogy, whereas quartz showed less. In this case, using the modal mineral composition of the rock as a proxy for surface area is a poor assumption. On the other hand, the Edwards carbonate showed a strong correlation between the modal mineral composition and the surface area. This suggests that the nature of a correlation, or lack thereof, will be rock specific. Further work is needed to see if these correlations can be related to the formation and diagenetic history of the rock.

**Table 8**
Mineral volume and specific surface area from X-ray CT. The porosities tabulated here are uncorrected for resolution. The heading *Area/bulk* means surface area per bulk volume of the sample.

| Specimen / porosity$^+$ | Group | Volume fraction | Surface area / bulk volume [$m^2$ / $m^3$] | Area fraction |
|---|---|---|---|---|
| Berea 1 | Clay | 4.8% | $1.56 \times 10^4$ | 37.5% |
| Plug 1 | Quartz | 89.5% | $2.17 \times 10^4$ | 52.2% |
| 16.0%$^+$ | Feldspar | 3.5% | $3.63 \times 10^3$ | 8.8% |
| | Others | 2.3% | $6.61 \times 10^2$ | 1.6% |
| | Total | 100.0% | $4.16 \times 10^4$ | 100.0% |
| Berea 1 | Clay | 2.5% | $5.50 \times 10^3$ | 17.0% |
| Plug 2 | Quartz | 77.4% | $1.93 \times 10^4$ | 59.5% |
| 11.4%$^+$ | Feldspar | 6.7% | $6.28 \times 10^3$ | 19.4% |
| | Others | 13.4% | $1.33 \times 10^3$ | 4.1% |
| | Total | 100.0% | $3.24 \times 10^4$ | 100.0% |
| Berea 1 | Clay | 1.3% | $2.83 \times 10^3$ | 10.5% |
| Plug 3 | Quartz | 74.7% | $1.87 \times 10^4$ | 68.8% |
| 9.8%$^+$ | Feldspar | 7.5% | $4.53 \times 10^3$ | 16.7% |
| | Others | 16.6% | $1.09 \times 10^3$ | 4.0% |
| | Total | 100.0% | $2.71 \times 10^4$ | 100.0% |
| Berea 1 | Clay | 3.7% | $9.76 \times 10^3$ | 21.4% |
| Plug 4 | Quartz | 86.4% | $3.05 \times 10^4$ | 67.0% |
| 16.2%$^+$ | Feldspar | 9.5% | $5.09 \times 10^3$ | 11.2% |
| | Others | 0.4% | $1.85 \times 10^2$ | 0.4% |
| | Total | 100.0% | $4.56 \times 10^4$ | 100.0% |
| Edwards | Quartz | 20.3% | $2.26 \times 10^4$ | 22.5% |
| 37.6%$^+$ | Dolomite | 78.6% | $7.61 \times 10^4$ | 75.5% |
| | Others | 1.1% | $2.03 \times 10^3$ | 2.0% |
| | Total | 100.0% | $1.01 \times 10^5$ | 100.0% |

### 3.3. The spatial distribution of surface area

For each rock five frequency histograms of the surface area distributions were generated. The histograms are provided for the Berea sandstone in Fig. 8 and for the carbonate rocks in Appendix F of the Supplemental Information.

Each histogram represents the distribution at a particular subsample size: 50, 75, 100, 200 and 300 μm respectively. Best fit log-normal (natural logarithm) curves are also shown on the histograms with their parameters, mean and standard deviation. The sixth graph in each figure shows box plots summarising the histogram data at each sub-volume length scale. On each box plot the central mark is the median, an x denotes the mean, the edges of the box are the 25th and 75th percentile, the whiskers mark 2.7 standard deviations and the red diamonds indicate outliers.

As the sampling size decreases the distributions broaden, reflecting the expected increase in heterogeneity at smaller sampling length scales. The distribution in the Berea sandstone and Estaillades carbonate are well described by a log-normal distribution whereas the remaining carbonates have more complex distributions. Multiple modes appear in the Guelph, Ketton, and Indiana carbonates.

Images of the digital rock subsamples at a length scale of 100 μm that have low, median and high values of the surface area to pore volume ratio are shown in Fig. 9 for samples of the Berea sandstone, and others are shown in Appendix F of the Supplemental Information. In all cases higher surface area to pore volume ratios are associated with more and smaller pores within the subvolume. Those subvolumes that are dominated by a single pore tend to have low surface areas. This is the kind of trend that is captured by simplified representations of surface area, e.g., the assumption of spheroid pores or mineral grains.

This description of surface area heterogeneity is less meaningful if the sub volume being used is smaller than a significant number of pores in the rock. This threshold can be seen clearly in Fig. 8 for the Berea sandstone where the mean in the surface area to pore volume ratio begins to deviate, generally increasing, when the sub-sample length decreases below the characteristic pore size of those rocks. The Berea sandstone has a single characteristic pore size and the distribution of surface area is not generally meaningful at size scales below this pore size. This issue is complicated, however, for rocks such as the carbonates in this work that have several modes or a continuous range of pore sizes across length scales. In this case surface area heterogeneity at small spatial scales in some locations in the rock may indeed be important simultaneous with regions of large spatial scale where the metric is meaningless because it is encompassed within a single pore body. In this case the multi-continuum formulation proposed by Lichtner and Kang (2007) may be appropriate.

A separate issue tied to the limitations in image resolution is that at small pore sizes, approaching single voxels, the marching cubes algorithm has trouble accurately interpolating and meshing the surfaces. As the sub volume scale decreases to 20 μm there is a large increase in surface area not accounted for. Thus statistics using the sub-volume sizes less than 50 μm were not included.

The distributions shown in Fig. 8 and in Appendix F of the Supplemental Information of the Berea sandstone and Edwards carbonate were further separated into the mineral groups obtained from the segmentation of the X-ray images. These rocks had significant fractions of multiple mineral groups, whereas the others were primarily calcite. These histograms are shown in Fig. 10 and in Appendix F of the Supplemental Information for the same range of sub-sample sizes with colours delineating each mineral group. Box plots summarising the mineral specific distributions at various sub

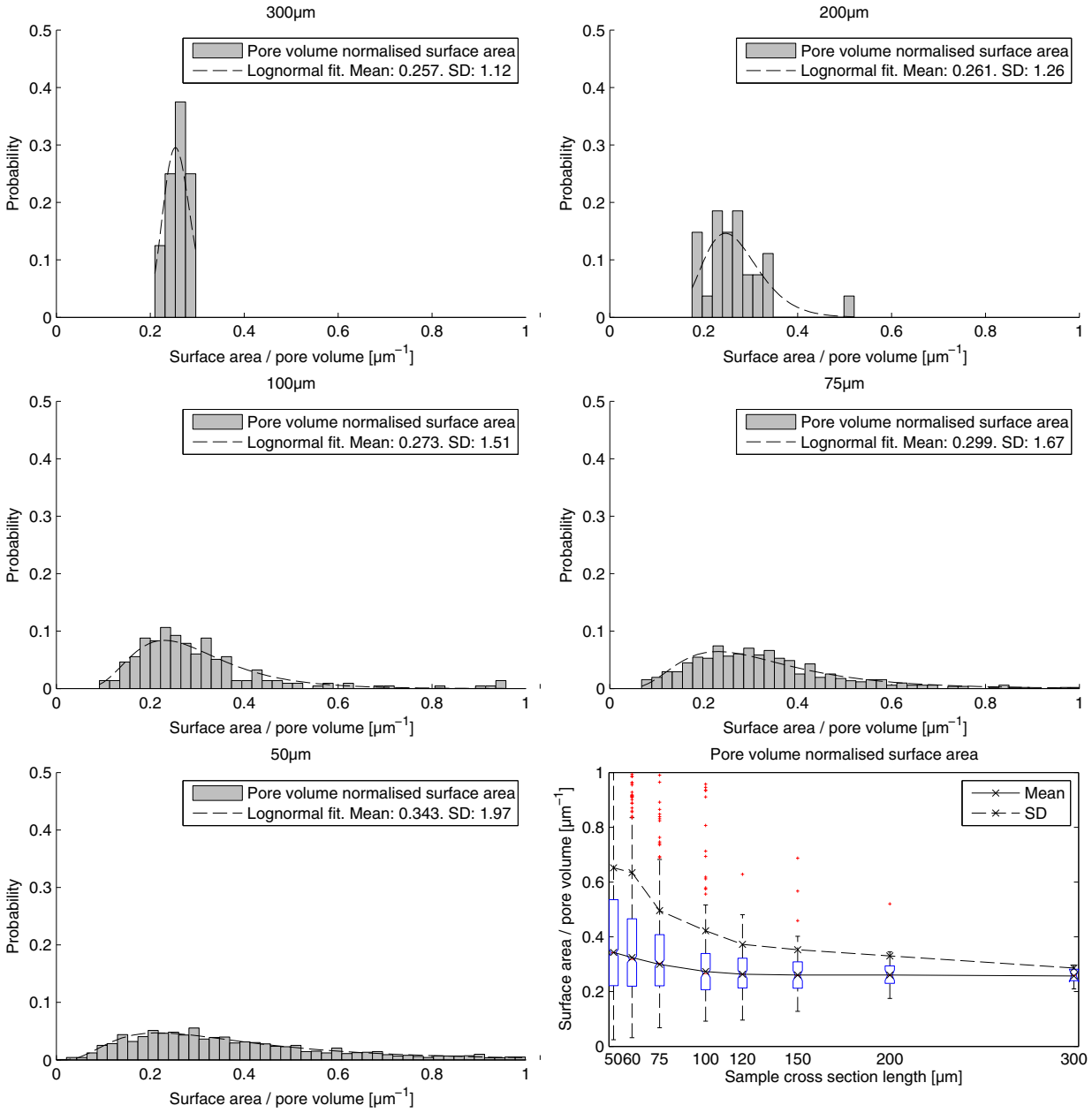


**Fig. 8.** Mono-mineralogical surface area distribution for Berea sandstone 1 plug 1.

volume sizes are also provided in Appendix F of the Supplemental Information.

The plots shown on a logarithmic scale showed that approximating the distributions as log normal appears to be appropriate for the Berea sandstone minerals and to a lesser degree with Edwards carbonate minerals. The log plots also show peaks at zero, indicative of sub-volume samples that have no surfaces associated with a given mineral. For example, in Fig. 10 at 200 μm, 7% of the sub-volume sample cubes do not have any of the feldspar group minerals in them.

Fig. 11 shows examples of 100 μm sub-volumes with the lowest, median and highest surface area to pore volume ratios obtained for the feldspar group. Images showing examples of the other groups are provided in Appendix Fin the Supplemental Information. Their respective surface area to pore volume measurements are included in the images. For the clay, feldspar and other group minerals of the Berea sandstone the most important factor determining the available surface was the overall abundance of the mineral itself in the sub-volume, rather than the geometry of the pores. For the quartz, the most important factor was the absence of other minerals and particularly clay. Thus the overall distribution of minerals at the scale of 100 μm generally determines the heterogeneity in surface area in the Berea sandstone. For the Edwards carbonate, the mineral groups were distributed more evenly at the scale of 100 μm, with nearly every sub-volume containing quartz and dolomite. In this case the surface area within a sub volume for a given mineral was the most important factor determining the mineral-specific surface area.

### *3.4. Analysis of the impact of surface area heterogeneity on reactive transport modelling*

Some insight into the impact of the observed heterogeneity on reactive transport processes can be obtained from the comparison of the

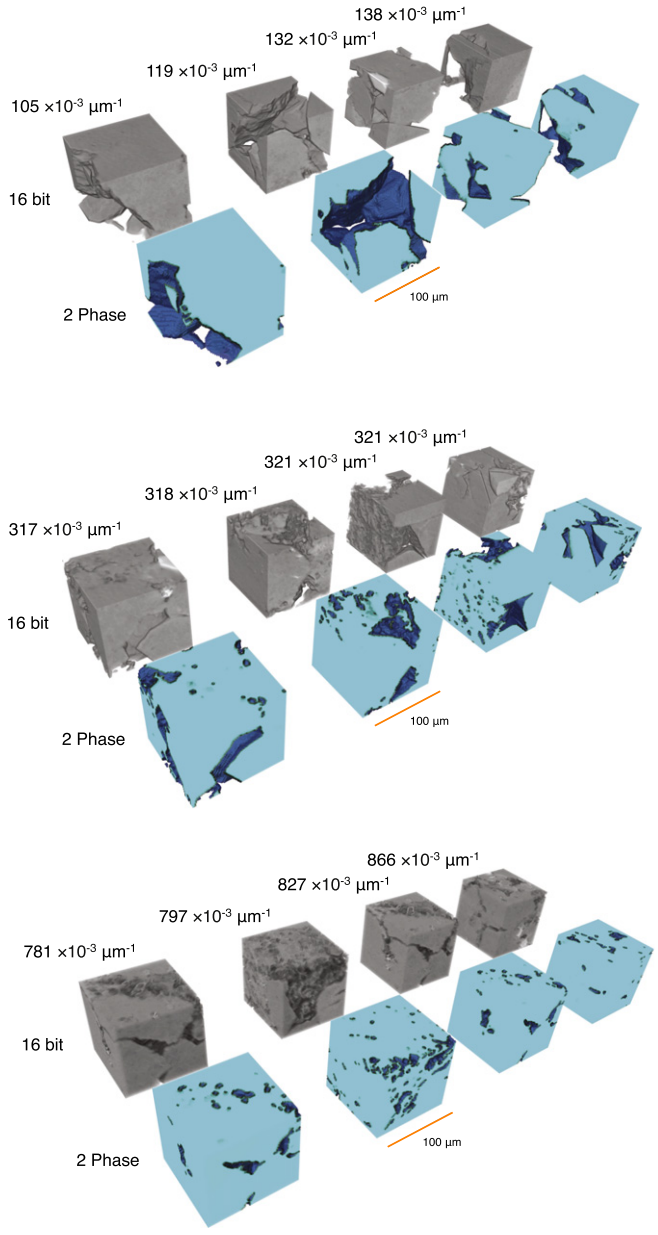


**Fig. 9.** Sub volume of Berea 1 plug 4 rock with binary segmentation showing from top to bottom: least, typical, and greatest surface area per pore volume.

observations presented here with the statistical properties assumed in past simulations focused on understanding the impact of surface area heterogeneity (Li et al., 2007; Peters, 2009; Nogues et al., 2013; Raoof et al., 2013). In particular, the pore network model simulations presented in Li et al. (2007) provide the best point of comparison because the mineralogical composition assumed in that work was broadly similar to the Berea sandstone in this study.

In that work, simulations were performed on a sandstone rock model composed of quartz, clay and anorthite, with the clay and anorthite constituting 6–50% of the volume fraction of the rock. The models with the lower fractions of reactive minerals (6.25 and 12.5%) were similar to the Berea sandstone used in this work. It was found that heterogeneity in the distribution of reactive surface area in the pore space could give rise to large deviations in effective reaction rates as compared with what would be predicted using continuum models with average parameters. At that time pore scale observations of the surface area properties were not available and the distributions were based on reasonable assumptions inferred from published values for $\approx 1$ cm$^3$ scale samples of various rocks, including Berea sandstone. The distribution of the surface area to pore volume in Li et al. (2007) was recreated and is shown in Fig. 12.

To make the comparison, the distributions of the Berea sandstone at the 100 µm subvolume size obtained in this study were used. The distributions had to be converted to values representative of those that would have been measured by BET adsorption to be comparable to the values used in Li et al. (2007), originally measured using BET. An accurate conversion depends on a characterisation of correlations between the geometric area of a mineral measured in the X-ray images and the observations with gas adsorption specific to those minerals which were unavailable for this work. Rather, we provide a first order estimate of what this conversion might look like based on surface area measurements of various mineral groups reported in the literature.

The average roughness ratio, $\beta$, of BET surface area, $A_{BET}$, to X-ray CT derived geometric surface area for Berea sandstone, $A_{geom}$, or

$$A_{BET} = \beta A_{geom}, \tag{2}$$

was found to be $\beta = 39$ as reported in Fig. 6. This roughness factor can be thought to be made up of contributions from the surfaces of specific minerals,

$$\beta = f_{qtz}\beta_{qtz} + f_{clay}\beta_{clay} + f_{fsp}\beta_{fsp} + f_{other}\beta_{other}, \tag{3}$$

where $f_i$ is the fraction of the geometric surface area made up of mineral group $i$, $\Sigma_i f_i = 1$ and $\beta_i$ are roughness ratios following the same relationship as shown in Eq. (2).

A first order estimate was made for this work from compiled literature values reported in (White et al., 1996). Those observations show that weathered quartz, feldspar, oxides and carbonates (these last two constituting the *other* grouping in this study) tend to have specific surface areas that are of the same order of magnitude whilst clays are a factor of 10 or more greater. Using the geometric surface area fractions of each mineral as the average from all datasets reported in Table 8, $\beta = 39$, and the constraints

$$\beta_{fsp} = \beta_{other} = \beta_{qtz} \tag{4}$$

$$\beta_{clay} = 10\beta_{qtz}, \tag{5}$$

Eq. (3) is reduced to an expression in $\beta_{qtz}$. Solving for this results in the roughness ratios, $\beta_{fsp} = \beta_{other} = \beta qtz = 13$ and $\beta_{clay} = 130$.

The geometric surface area fraction of each mineral group is shown in a stacked bar plot in Appendix G of the Supplemental Information. There was no apparent correlation between the total amount of surface area and the surface area abundance of each mineral group, e.g., clay was not more or less abundant at the pore surfaces of those sub volumes with higher or lower surface area to pore volume ratios. Using the roughness ratios and the mineral surface composition, a roughness factor for each sub volume was calculated and used to convert the geometric surface area distribution to a BET equivalent surface area distribution.

A compilation of histogram plots is shown in Fig. 12 which includes the distribution of $\beta$ values for all of the sub volumes, the surface area to pore volume distribution observed in this work before and after normalisation to BET equivalent values, and the distribution assumed in Li et al. (2007), based on observations made with BET adsorption. The distribution in $\beta$ reflects the range of modal composition of the pore–solid interface of the sub volumes, generally dominated by quartz (low $\beta$ values) but with a significant number of pores where clay dominates the surface area composition. The conversion of the geometric surface area distribution to the BET equivalent results in a skew of the distribution giving it a more exponential character as compared to the lognormal shape of the geometric surface area distribution. The variance also increases relative to the value of the mean. The distribution of the surface area to pore

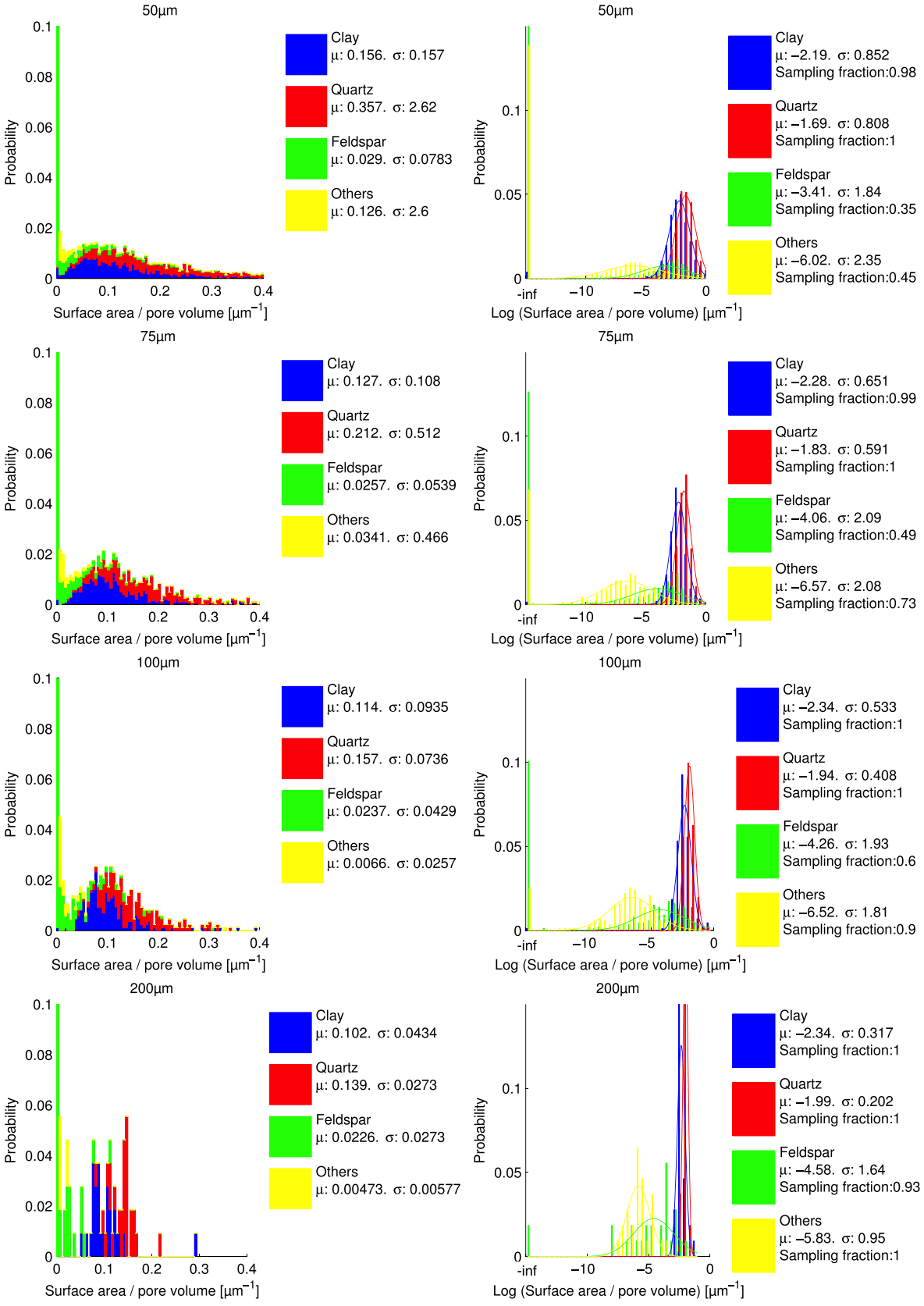


**Fig. 10.** Multi-mineralogical surface area distribution for Berea 1 plug 1. The right columns show the data on a natural logarithm plot.

volume ratio implied in Li et al. (2007) is more heterogeneous than what was observed in this work, with a variance an order of magnitude higher than the variance obtained in the BET equivalent distribution.

Changing the roughness factor for clay can only moderately increase the variance due to the constraint that the bulk value for $\beta = 39$ as measured. This results in tradeoffs in roughness factors between minerals, as

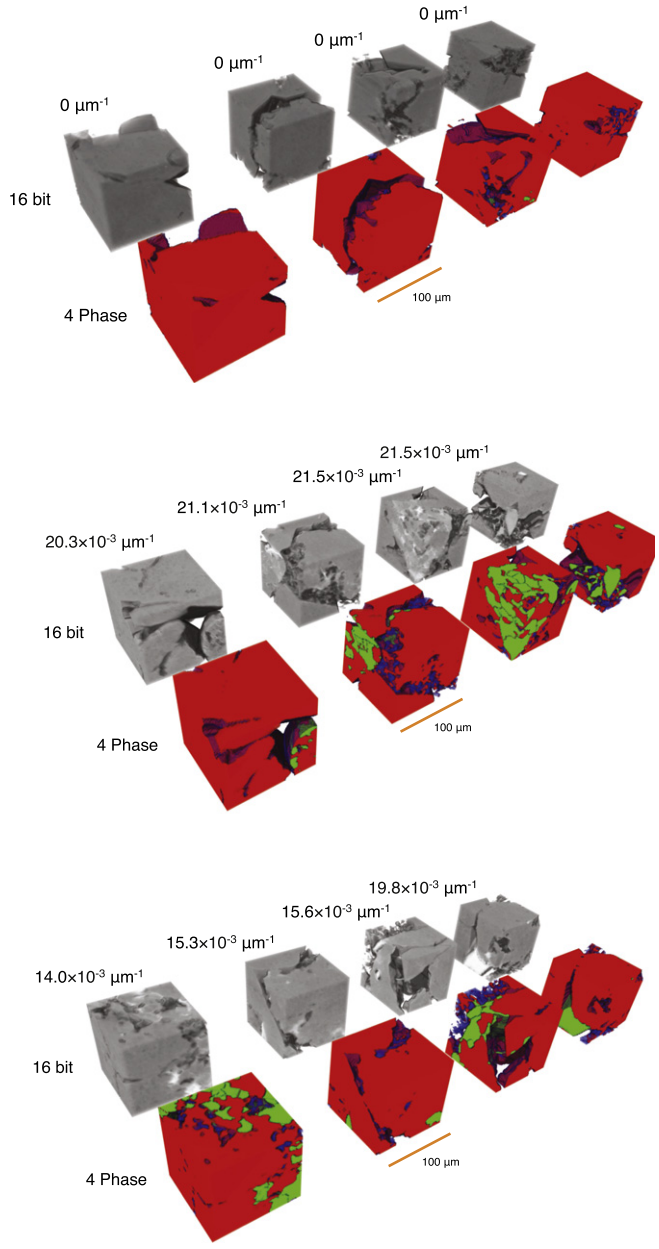


**Fig. 11.** Sub volumes of the Berea sandstone with 5 phase segmentation showing from top to bottom: least, greatest, and typical *feldspar* surface area per pore volume. The colour scheme is the same as in Fig. 10. Similar images focused on the other mineral groups and for the Edwards carbonate are included in Appendix F of the Supplemental Information.

implied by the constraints of Eq. (4) and (5). Increasing the clay roughness factor only does so relative to quartz, which is reduced to maintain the constraint $\beta = 39$. In other words, given the observations of bulk average specific surface area, bulk mineral composition at the surfaces of the pores and minimal porosity below the resolution of the X-ray images, there are important limits to the surface area that one could assume exists in, e.g., a completely clay lined pore. Additionally, values of $\beta$ cannot be reasonably assumed to be less than one, further limiting the range of roughness available.

The difference in the distributions appeared to originate predominantly in the assumption common to pore network model studies that surface area and pore volumes for a given pore are uncoupled. There was a weak positive correlation of surface area with pore volume shown in Fig. 13a. The surface area to pore volume ratios fell between the bounds of the ratio that would be obtained for spheres with the quartz roughness factor ($\beta = 13$) and five times that of spheres with the clay roughness factor ($\beta = 130$). Note that the quartz boundary is a theoretical minimum limit whereas the clay boundary is not a theoretical upper limit.

Fig. 13b shows an uncorrelated realisation of the plot — surface areas were plotted randomly against pore volumes from the set of subvolumes to evaluate the impact of this assumption. The ratio of surface area to pore volume falls well outside of the boundaries observed, with both very large surface areas and surface areas smaller than the theoretical minimum for a given pore volume. This resulted in a significant widening of the distribution of surface area to pore volume, shown in Fig. 12e and in a cumulative distribution plot in Appendix H of the Supplemental Information.

## 4. Discussion and conclusions

We do not currently have general rules to determine the relevant size scales at which heterogeneity should be characterised for accurate and practical modelling of processes of reactive flow. This will depend ultimately on the length scale over which heterogeneity in the overall reaction rate may appear. Reaction rate heterogeneity may develop because of heterogeneity in the distribution of reactive surfaces, but heterogeneity in the fluid chemical composition, local flow rates and temperature can be of equal or greater importance depending on the specific setting (Li et al., 2007; Flukiger and Bernard, 2009; Molins et al., 2012). Further, the relative influences of these processes are coupled (surface area giving rise to reaction heterogeneity will lead to heterogeneity in local chemical composition and so on), and the relevant scale at which to characterise surface area heterogeneity may be highly process-specific. This work provides a statistical characterisation of pore scale heterogeneity in the reactive surface area of minerals within permeable rocks based on direct observation of the pore morphology and mineral distribution in three dimensions.

Comparison of average specific surface area from BET measurements with those inferred from X-ray images showed that the two observations could be reconciled with a variation on the use of a roughness factor, $\beta$. Roughness factors ranged from $10 < \beta < 200$. Total BET surface area, the presence of clay, and microporosity were all associated with higher values of the roughness factor for a given rock.

Average mineral composition computed from X-ray images corresponded well with the average composition obtained from segmented BSE images. In the Berea sandstone, clays preferentially coated quartz grains and resulted in no correlation between the modal mineral composition of the rock and the fraction of surface area made up by the mineral. In situations like this, using the mineral composition of the rock as a proxy for surface area would lead to significant error in reaction modelling. On the other hand, the volumetric composition and surface area fraction in the Edwards carbonate were strongly correlated. In cases like this, the assumption is reasonable.

Distributions of the surface area to pore volume ratio were presented as a measure of heterogeneity of the reactive surface area in the rocks. In sandstone and carbonate rocks high values of the ratio were associated with a larger number of volumetrically smaller pores. Locations in the rock with larger pores tended to have lower surface area to pore volume ratios.

Distributions of this ratio for specific mineral groups in Berea sandstone and Edwards carbonate were constructed. In the Berea sandstone, the most important factor determining abundance of the surface area of clay and feldspar group minerals in a location was the presence of the mineral in that location — increased feldspar led to increased feldspar surface area. For quartz, however, the presence or absence of clay was the most important factor. In the Edwards carbonate, the amount of total surface area within a sub volume was the most important factor controlling the abundance of the surface area of a given mineral group.

The information can be used directly in statistically-based models of reactive transport including the emerging group of pore network models focused on characterising reactive processes. In pore network

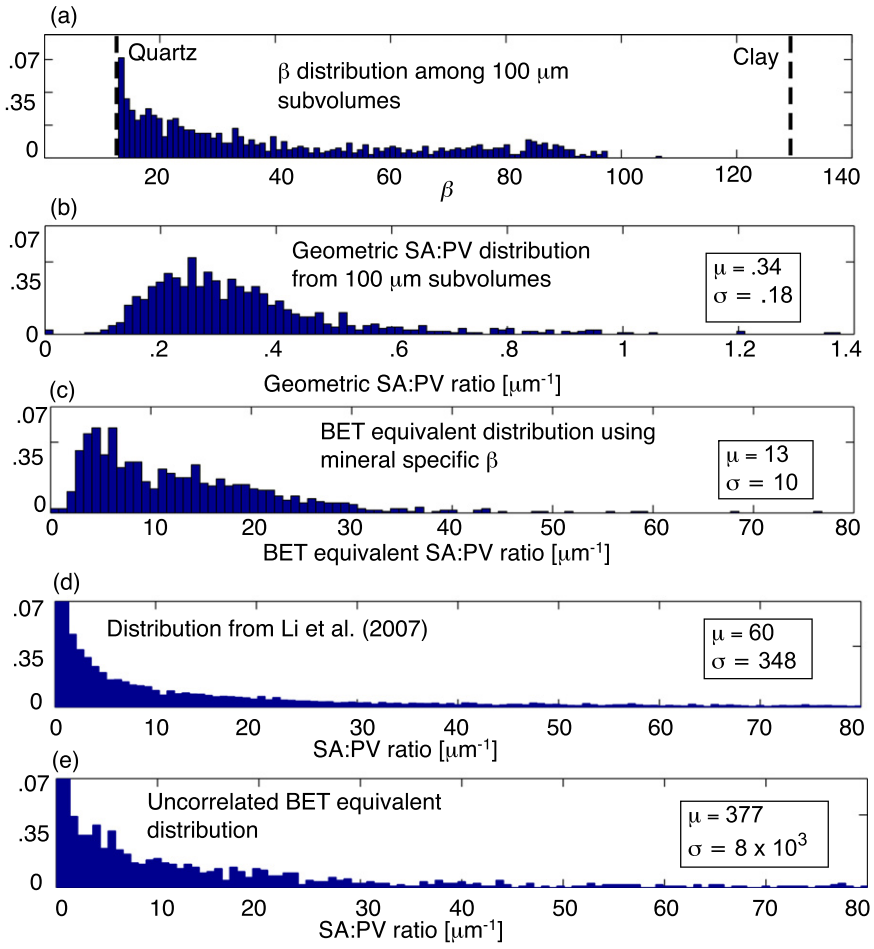


**Fig. 12.** (a) The distribution of roughness factors calculated for each specific 100 μm sub volume from all of the Berea sandstone samples (see Section 4). (b) The compiled surface area to pore volume distribution for the Berea sandstone observations calculated from X-ray imagery. (c) The conversion of the geometric surface area distribution to a BET equivalent surface area distribution using roughness factors shown in the top plot. (d) The distribution of surface area to pore volume used in the work of Li et al. (2007). (e) The distribution obtained from the observations in this work randomly associating the surface area of a subvolume to the pore volume of a subvolume. For the last two plots note that the horizontal axis of the final plot is cut off so as to provide a visual comparison. The variance and mean indicate the length of the tail and the distribution function with longer axes are shown in Appendix H of the Supplemental Information.

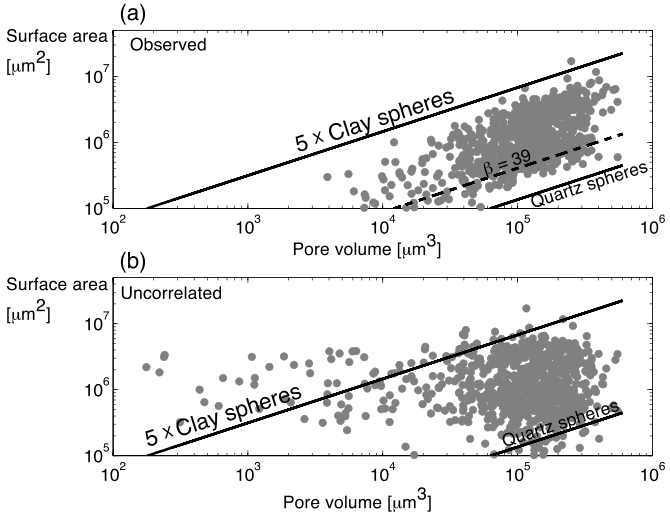


**Fig. 13.** This figure shows two plots of the BET normalised surface area calculated from the X-ray imagery against the pore volume for 900 subsamples ($10^6$ μm$^3$) of an X-ray image. (a) The observed properties–surface area and pore volume were obtained from the same subvolume. (b) The impact of removing the correlation in the properties–surface areas were plotted randomly against pore volumes from the set of subvolumes. The lines show the values that would be obtained for spheres with five times the clay roughness factor ($\beta = 130$), the average roughness factor ($\beta = 39$), and the quartz roughness factor ($\beta = 13$) which is a theoretical minimum for these observations.

models it will be important to put physically based constraints on combinations of properties for individual pores. In this work it was found that combinations of pore volume and surface area for a specific pore were constrained to values ranging between five times those that would be obtained for clay lined spheres and those that would be obtained for quartz lined spheres.

## Acknowledgments

The authors wish to thank the four reviewers and the Editor-in-chief who provided extensive reviews which led to a substantially improved manuscript.

The authors gratefully acknowledge funding support for this work from the Qatar Carbonates and Carbon Storage Research Centre (490000724) at Imperial College London provided jointly by Shell, Qatar Petroleum and the Qatar Science and Technology Park. The authors also acknowledge mercury intrusion data on Berea sandstone kindly provided by Ali Al-Menhali, and nitrogen porosimetry data on carbonate samples kindly provided by Ben Niu and Norman Nicholls.

## Appendix A. Supplementary data

Supplementary data to this article can be found online at http://dx.doi.org/10.1016/j.chemgeo.2015.07.010.

## References


Bijeljic, B., Mostaghimi, P., Blunt, M.J., 2013. Insights into non-fickian solute transport in carbonates. Water Resour. Res. 49, 2714–2728.

Boso, F., Battiato, I., 2013. Homogenizability conditions for multicomponent reactive transport. Adv. Water Resour. 62, 254–265.

Cadoret, T., Marion, D., Zinszner, B., 1995. Influence of frequency and fluid distribution on elastic wave velocities in partially saturated limestones. J. Geophys. Res. 100, 9789–9803.

Churcher, P.L., French, P.R., Shaw, J.C., Schramm, L.L., 1991. Rock Properties of Berea Sandstone, Baker Dolomite, and Indiana Limestone.

Colon, C.F.J., Oelkers, E.H., Schott, J., 2004. Experimental investigation of the effect of dissolution on sandstone permeability, porosity, and reactive surface area. Geochim. Cosmochim. Acta 68, 805–817.

Dentz, M., Borgne, T., Englert, A., Bijeljic, B., 2011. Mixing, spreading and reaction in heterogeneous media: a brief review. J. Contam. Hydrol. 120–121, 1–17.

Ethington, E.F., 1990. Interfacial Contact Angle Measurements of Water, Mercury, and 20 Organic Liquids on Quartz, Calcite, Biotite, and Ca-Montmorillonite Substrates.

Flukiger, F., Bernard, D., 2009. A new numerical model for pore scale dissolution of calcite due to $CO_2$ saturated water flow in 3D realistic geometry: principles and first results. Chem. Geol. 265, 171–180.

Golab, A., Romeyn, R., Averdunk, H., Knackstedt, M., Senden, T.J., 2013. 3D characterisation of potential $CO_2$ reservoir and seal rocks. Aust. J. Earth Sci. 60, 111–123.

Gouze, P., Luquot, L., 2011. X-ray microtomography characterization of porosity, permeability and reactive surface changes during dissolution. J. Contam. Hydrol. 120–121, 45–55.

Haggerty, R., Gorelick, S.M., 1995. Multiple-rate mass transfer for modeling diffusion and surface reactions in media with pore-scale heterogeneity. Water Resour. Res. 31, 2383–2400.

Hanchen, M., Krevor, S., Mazzotti, M., Lackner, K., 2007. Validation of a population balance model for olivine dissolution. Chem. Eng. Sci. 62, 6412–6422.

Helgeson, H.C., Murphy, W.M., Aagaard, P., 1984. Thermodynamic and kinetic constraints on reaction rates among minerals and aqueous solutions. II. Rate constants, effective surface area, and the hydrolysis of feldspar. Geochim. Cosmochim. Acta 48, 2405–2432.

Hezel, D.C., Elangovan, P., Viehmann, S., Howard, L., Abel, R., Armstrong, R., 2013. Visualisation and quantification of CV chondrite petrography using micro-tomography. Geochim. Cosmochim. Acta 116, 33–40.

Kampman, N., Bickle, M., Becker, J., Assayag, N., Chapman, H., 2009. Feldspar dissolution kinetics and Gibbs free energy dependence in a CO2-enriched groundwater system, Green River, Utah. Earth Planet. Sci. Lett. 284, 473–488.

Kerbrat, M., Pinzer, B., Huthwelker, T., Gaggeler, H., Ammann, M., Schneebeli, M., 2008. Measuring the specific surface area of snow with x-ray tomography and gas adsorption: comparison and implications for surface smoothness. Atmos. Chem. Phys. 8, 1261–1275.

Khilar, K., Fogler, H., 1983. Water sensitivity of sandstones. Soc. Pet. Eng. 23, 55–64.

Kieffer, B., Colon, C.F.J., Oelkers, E.H., Schott, J., 1999. An experimental study of the reactive surface area of the fontainbleau sandstone as a function of porosity, permeability, and fluid flow rate. Geochim. Cosmochim. Acta 63, 3525–3534.

Knackstedt, M., Sok, R., Sheppard, A., Latham, S., Madadi, M., Varslot, T., Arns, C., Bächle, G., Eberli, G., 2008. Probing pore systems in carbonates: correlations to petrophysical properties.

Landrot, G., Ajo-Franklin, J.B., Yang, L., Cabrini, S., Steefel, C., 2012. Measurement of accessible reactive surface area in a sandstone, with application to $CO_2$ mineralization. Chem. Geol. 318–319, 113–125.

Latham, S., Varslot, T., Sheppard, A., 2008. Image registration: enhancing and calibrating X-ray micro-CT imaging. Soc. Core Anal. 35, 1–12.

Li, L., Peters, C.A., Celia, M.A., 2007. Applicability of averaged concentrations in determining geochemical reaction rates in heterogeneous porous media. Am. J. Sci. 307, 1146–1166.

Lichtner, P., Kang, Q., 2007. Upscaling pore-scale reactive transport equations using a multiscale continuum formulation. Water Resour. Res. 43, W12S15.

Luquot, L., Gouze, P., 2009. Experimental determination of porosity and permeability changes induced by injection of $co_2$ into carbonate rocks. Chem. Geol. 265, 148–159.

Maher, K., Steefel, C.I., DePaolo, D.J., Viani, B.E., 2006. The mineral dissolution rate conundrum: insights from reactive transport modeling of U isotopes and pore fluid chemistry in marine sediments. Geochim. Cosmochim. Acta 70, 337–363.

Malmström, M.E., Destouni, G., Banward, S.A., Strömberg, B.H., 2000. Resolving the scale-dependence of mineral weathering rates. Environ. Sci. Technol. 34, 1375–1378.

Menke, H.P., Bijeljic, B., Andrew, M.G., Blunt, M.J., 2015. Dynamic Three-Dimensional Pore-Scale Imaging of Reaction in a Carbonate at Reservoir Conditions. Environ. Sci. Technol. 49 (7), 4407–4414.

Molins, S., Trebotich, D., Steefel, C.I., Shen, C., 2012. An investigation of the effect of pore scale flow on average geochemical reaction rates using direct numerical simulation. Water Resour. Res. 48.

Navarre-Sitchler, A., Brantley, S.L., 2007. Basalt weathering across scales. Earth Planet. Sci. Lett. 261, 321–334.

Navarre-Sitchler, A., Cole, D., Rother, G., Jin, L., Buss, H., Brantley, S., 2013. Porosity and surface area evolution during weathering of two igneous rocks. Geochim. Cosmochim. Acta 109, 400–413.

Nogues, J.P., Fitts, J.P., Celia, M.A., Peters, C.A., 2013. Permeability evolution due to dissolution and precipitation of carbonates using reactive transport modeling in pore networks. Water Resour. Res. 49, 6006–6021.

Noiriel, C., Luquot, L., Madé, B., Raimbault, L., Gouze, P., Le, J.v.d., 2009. Changes in reactive surface area during limestone dissolution: an experimental and modelling study. Chem. Geol. 265, 160–170.

Peters, C.A., 2009. Accessibilities of reactive minerals in consolidated sedimentary rock: an imaging study of three sandstones. Chem. Geol. 265, 198–208.

Raoof, A., Nick, H.M., Hassanizadeh, S.M., Spiers, C.J., 2013. PoreFlow: a complex pore-network model for simulation of reactive transport in variably saturated porous media. Comput. Geosci. 61, 160–174.

Sen, P.N., Straley, C., Kenyon, W.E., Whittingham, M.S., 1990. Surface-to-volume ratio, charge density, nuclear magnetic relaxation, and permeability in claybearing sandstones. Geophysics 55, 61–69.

Shaw, J.C., Churcher, P.L., Hawkins, B.F., 1991. The effect of firing on berea sandstone. SPE Form. Eval. 6, 72–78.

Sok, R.M., Varslot, T., Ghous, A., Latham, S., Sheppard, A.P., Knackstedt, M.A., 2010. Pore scale characterization of carbonates at multiple scales: Integration of micro-CT, BSEM and FIBSEM. Petrophysics 51, 379.

Steefel, C., Maher, K., 2009. Fluid-rock interaction: a reactive transport approach. Rev. Mineral. Geochem. 70, 485–532.

Steefel, C., Depaolo, D., Lichtner, P., 2005. Reactive transport modeling: an essential tool and a new research approach for the Earth sciences. Earth Planet. Sci. Lett. 240, 539–558.

Tsuchiyama, A., Hanamoto, T., Nakashima, Y., Nakano, T., 2000. Quantitative evaluation of attenuation contrast of minerals by using a medical X-ray CT scanner. J. Mineral. Petrol. Sci. 95, 125–137.

Tsuchiyama, A., Uesugi, K., Nakano, T., Ikeda, S., 2005. Quantitative evaluation of attenuation contrast of X-ray computed tomography images using monochromatized beams. Am. Mineral. 90, 132–142.

Tsuchiyama, A., Nakano, T., Uesugi, K., Uesugi, M., Takeuchi, A., Suzuki, Y., Noguchi, R., Matsumoto, T., Matsuno, J., Nagano, T., Imai, Y., Nakamura, T., Ogami, T., Noguchi, T., Abe, M., Yada, T., Fujimura, A., 2013. Analytical dual-energy microtomography: a new method for obtaining three-dimensional mineral phase images and its application to Hayabusa samples. Geochim. Cosmochim. Acta 116, 5–16.

Uesugi, K., Tsuchiyama, A., Nakano, T., Suzuki, Y., Yagi, N., Umetani, K., Kohmura, Y., 1999. Development of microtomography imaging system for rock and mineral samples. SPIE Int. Symp. Opt. Sci. Eng. Instrum. 3772, 214–221.

Velbel, M.A., 1985. Geochemical mass balances and weathering rates in forested watersheds of the southern blue ridge. Am. J. Sci. 285, 904–930.

White, A.F., Brantley, S.L., 2003. The effect of time on the weathering of silicate minerals: why do weathering rates differ in the laboratory and field? Chem. Geol. 202, 479–506.

White, A.F., Peterson, M.L., 1990. Role of reactive-surface-area characterization in geochemical kinetic models. ACS Symp. Ser. 416, 461–475.

White, A.F., Blum, A.E., Schulz, M.S., Bullen, T.D., Harden, J.W., Peterson, M.L., 1996. Chemical weathering rates of a soil chronosequence on granitic alluvium: I. Quantification of mineralogical and surface area changes and calculation of primary silicate reaction rates. Geochim. Cosmochim. Acta 60, 2533–2550.

Zhu, C., 2005. In situ feldspar dissolution rates in an aquifer. Geochim. Cosmochim. Acta 69, 1435–1453.